Isoscalar giant resonances in ^{90,92,94}Zr

Krishichayan,[1,2,*] Y.-W. Lui,[3] J. Button,[3] D. H. Youngblood,[3] G. Bonasera,[3] and S. Shlomo[3]
[1]*Department of Physics, Duke University, Durham, North Carolina 27708, USA*
[2]*Triangle Universities Nuclear Laboratory, Durham, North Carolina 27708, USA*
[3]*Cyclotron Institute, Texas A&M University, College Station, Texas 77843, USA*
(Received 1 September 2015; published 23 October 2015)

Isoscalar giant resonances in ^{90,92,94}Zr have been studied with inelastic scattering of 240 MeV α particles at small angles including 0°. A significant fraction of the energy-weighted sum rule (EWSR) was found for isoscalar $E0$ (106%,103%,106%), $E1$ (64%,53%,96%), $E2$ (92%,93%,67%) and high energy octupole $E3$ (59%,69%,58%) resonances in ^{90,92,94}Zr respectively. Hartree-Fock random phase approximation (RPA) calculations were made for each multipole using the KDE0v1 Skyrme-type effective nucleon-nucleon interaction and the results are compared to the experimental distributions.

DOI: 10.1103/PhysRevC.92.044323 PACS number(s): 25.55.Ci, 24.30.Cz, 27.60.+j

I. INTRODUCTION

The giant resonances are small amplitude collective modes of excitation of nuclei and have been extensively studied since the discovery of the isovector giant dipole resonance (IVGDR) in 1947 by Baldwin and Klaiber [1]. Twenty-five years later, Pitthan and Walcher [2] reported a structure at $E_x \sim 63/A^{1/3}$ MeV seen in inelastic electron scattering, having a q dependence consistent with an $E2$ or $E0$ excitation, and suggested it might be an isoscalar giant quadrupole resonance (ISGQR); however, electron scattering strongly excites both isoscalar and isovector states. A study of inelastic α scattering from ^{40}Ca by Rutledge and Hiebert [3] confirmed the isoscalar nature of the peak at $E_x \sim 63/A^{1/3}$ MeV in ^{40}Ca, and from the angular distribution that it would be an $E2$ or $E0$ resonance. A study of 15 nuclei from ^{24}Mg to ^{208}Pb with inelastic α scattering by Moss *et al.* [4] confirmed the existence of this resonance in many nuclei with A $\geqslant$ 40, with 50–100% of the $E2$ energy-weighted sum rule (EWSR). If the peak were the isoscalar giant monopole resonance (ISGMR), it would require ∼300% of the $E0$ EWSR. The first experimental results suggesting the existence of an ISGMR at about the same energy as the IVGDR were reported by Marty *et al.* in 1975 using inelastic scattering of deuterons [5] to study ^{40}Ca, ^{90}Zr, and ^{208}Pb; however, they could not distinguish $E0$ and $E2$. Subsequently, analysis of electron scattering data [6] and α scattering data [7] confirmed strength at $\sim 80/A^{1/3}$ MeV, but could not distinguish $E0$ from $E2$ or $E4$. In 1977, Youngblood *et al.* [8] using inelastic scattering of α particles at small angles, where an $E0$ angular distribution will have a sharp dip that is not present in an $E2$ distribution, and showed that the $E_x \sim 80/A^{1/3}$ MeV peaks in ^{144}Sm and ^{208}Pb were the ISGMR, exhausting ∼100% of the $E0$ EWSR, while the $E_x \sim 63/A^{1/3}$ MeV peak was the ISGQR.

Using electron scattering, Nagao and Torizuka [9] in 1973 reported the observation of an isoscalar octupole state in ^{208}Pb at $E_x \sim 19$ MeV exhausting 44% of the $E3$ EWSR. Seven years later, Carey *et al.* [10], using 800 MeV protons, reported identifying an octupole resonance in ^{40}Ca, ^{116}Sn, and ^{208}Pb at about $E_x = 110/A^{1/3}$ MeV, while Morsch *et al.* [11] using 152 MeV α particles reported both an octupole resonance at $E_x = 17.5$ MeV and an isoscalar dipole resonance at $E_x = 21.3$ MeV in ^{208}Pb. In 1976, Moss *et al.* [12] using inelastic scattering of α particles, identified the $1\hbar\omega$ component of the isoscalar octupole giant resonance at $E_x \sim 32/A^{1/3}$ MeV in seven medium mass nuclei. Subsequently, the $1\hbar\omega$ component has been referred to as the low energy octupole resonance (LEOR), while the higher ($3\hbar\omega$) component is referred to as the high energy octupole resonance (HEOR).

The ISGMR, in which protons and neutrons in a nucleus move in-phase and oscillate with spherical symmetry, is particularly important as it provides information about the incompressibility of the nucleus, K_A, from which the incompressibility of infinite nuclear matter, K_{NM}, can be obtained [13,14]. The incompressibility of a nucleus (K_A) is related to the ISGMR energy by $K_A = [M/\hbar^2]\langle r^2\rangle E^2_{\rm GMR}$ where in the scaling model $E_{\rm GMR} = (m_3/m_1)^{1/2}$, $m_k = \sum_n (E_n - E_0)^k |\langle 0|r^2|n\rangle|^2$ is the kth moment of the strength distribution, and M is the nucleon mass.

The Texas A&M group studied the ISGMR in a large number of nuclei having $12 \leqslant A \leqslant 208$ [15–19] using 240 MeV α inelastic scattering measured at small angles including 0°. The monopole strength in heavier (spherical) nuclei was found to be concentrated in a mostly symmetrical peak, and in light nuclei the strength is located either in a peak with significant tailing to the high energy side or with obvious broad components above the main peak [16,17,20]. The mass 90 region is a transitional region for the giant monopole resonance. The ISGMR strength in ^{90}Zr is contained largely in a symmetric peak, but with a tail on the high excitation side [21]. This discovery resolved an issue where the interactions which reproduced the energies of the ISGMR in heavier nuclei gave an ISGMR position in ^{90}Zr well above the centroid of the peak containing the bulk of the ISGMR strength [21]. We have explored the ISGMR strength distribution in Zr isotopes and Mo isotopes and reported those results [15]. Because of the excellent peak-to-continuum ratio [22,23] with the 240 MeV α data, the actual distribution of strength between $E_x = 9$ and 36 MeV can be obtained not only for the ISGMR but

*krishi@tunl.duke.edu and krishichayan@gmail.com

for the isoscalar giant dipole resonance (ISGDR), ISGQR, and HEOR as well. In this paper, we report the $E0$–$E3$ multipole strength distributions obtained for ^{90,92,94}Zr and compare them to Hartree-Fock randon phase approximation (HF-RPA) calculations [24] with the KDE0v1 Skyrme-type effective interactions [25]. The KDE0v1 interaction was found to be consistent with our current knowledge of properties of nuclei, nuclear matter, and neutron stars (see Sec. IV).

II. EXPERIMENTAL TECHNIQUE AND DATA ANALYSIS

The experimental technique and detailed method of the analysis have been discussed thoroughly in Refs. [22,26,27] and are summarized briefly below. A beam of 240 MeV α particles from the Texas A&M K500 superconducting cyclotron, after passing through a beam analysis system, bombarded self-supporting target foils 5–8 mg/cm^2 thick enriched to more than 96% in the desired isotope and located in the scattering chamber of the multipole-dipole-multipole (MDM) spectrometer. The horizontal acceptance of the spectrometer was 4° and the vertical acceptance was set at ±2°. Ray tracing was used to reconstruct the scattering angle. Scattered particles entering the MDM spectrometer were momentum analyzed and measured by a 60 cm long focal plane detector, which consisted of four resistive wire proportional counters to measure position as well as an ionization chamber to provide ΔE and a plastic scintillator behind the ionization chamber to measure the energy deposited, and provided a fast timing signal for each event. A position resolution of ∼0.9 mm and scattering angle resolution of ∼0.09° were obtained. The energy resolution in the giant resonance region was ∼250 keV. The out-of-plane scattering angle was not measured. At $\theta_{\rm spec} = 0°$, runs with an empty target frame had an α-particle rate approximately 1/2000th of that with a target in place, and α particles were uniformly distributed in the spectrum. The target thicknesses were measured by weighing and checked by measuring the energy loss of the 240 MeV α beam in each target. The data for each run were binned into ten angle bins by horizontal angle. The scattering angle for each angle bin was obtained by integrating over the vertical opening of the slit. The differential cross section was extracted from the number of beam particles collected, the target thickness, the solid angle, the yields measured, and the dead time. The number of beam particles was monitored with a monitor detector at a fixed scattering angle in the scattering chamber. Dead time of the data acquisition system was measured by comparing the number of pulses sent to the system to those accepted. The cumulative uncertainties in the above parameters result in an approximately ±10% uncertainty in absolute cross sections. ^{24}Mg spectra were taken before and after each run, and the 13.85 ±0.02 MeV $L = 0$ state [28] was used as a check on the energy calibration in the giant resonance region.

Giant resonance (GR) data were taken with the spectrometer at 0.0° (0.0° < θ < 2.0°) and at 4.0° (2.0° < θ < 6.0°). Sample spectra obtained for ^{90,92,94}Zr are shown in Fig. 1. The giant resonance peaks can be seen extending up past $E_x = 30$ MeV in all nuclei. The spectra were divided into a peak and a continuum where the continuum was assumed to have the shape of a straight line at high excitation joining onto a Fermi shape at low excitation to model particle threshold effects [22]. Samples of the continua used in the analysis are shown in Fig. 1.

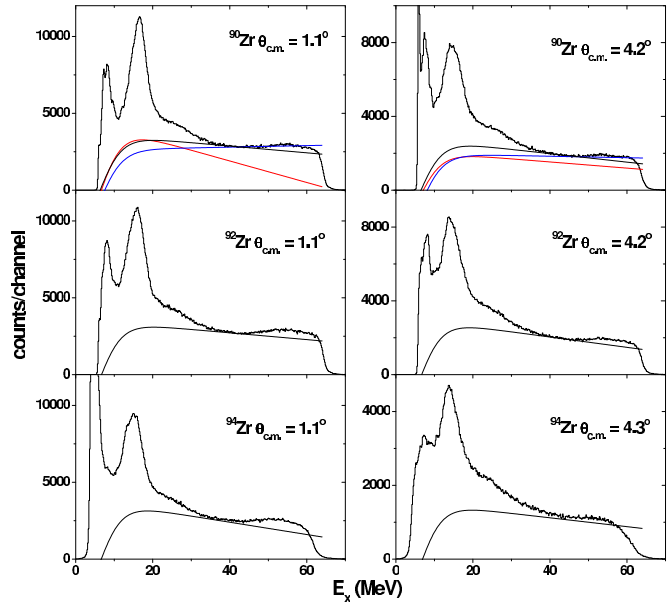

FIG. 1. (Color online) Inelastic α spectra obtained for ^{90,92,94}Zr. The lines indicate continuum choices, with the variety of choices shown by the different lines in the ^{90}Zr spectra.

III. MULTIPOLE ANALYSIS

The mulitpole components of the giant resonance peak were obtained [22,26,27] by dividing the peak into multiple regions (bins) by excitation energy and then comparing the angular distributions obtained for each of these bins to distorted wave Born approximation (DWBA) calculations. The uncertainty from the multipole fits was determined for each multipole by incrementing (or decrementing) that strength, then adjusting the strengths of the multipoles to minimize total χ^2. This continued until the new χ^2 was one unit larger than the total χ^2 obtained for the best fit. Optical parameters for the calculations were determined from elastic scattering for ^{90}Zr [29] and are given in Table I along with Fermi parameters used for the density distribution of the nuclear ground state.

The DWBA calculations were performed [30,31] using the density-dependent single-folding model for the real part, obtained with a Gaussian α-nucleon potential, and a phenomenological Woods-Saxon potential for the imaginary term. The α-nucleus interaction is given by

$$U(r) = V_F(r) + iW/\{1 + \exp[(r - R_i)/a_i]\}, \qquad (1)$$

TABLE I. Optical and Fermi parameters used in DWBA calculations [29].

V (MeV)	W_i (MeV)	r_i (fm)	a_i (fm)	c (fm)	a (fm)
40.2	40.9	0.786	1.242	4.901	0.515

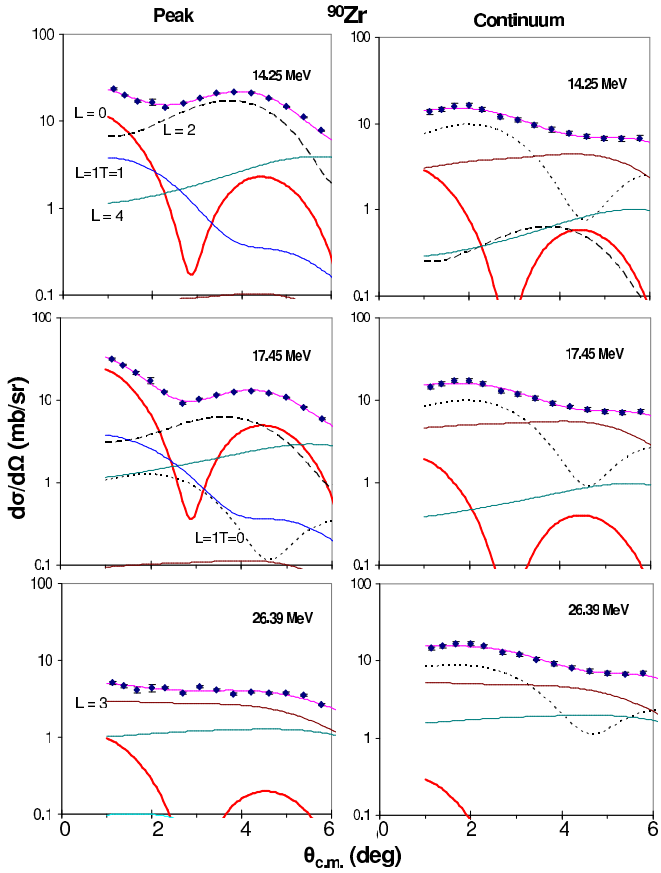

FIG. 2. (Color online) The angular distributions of the ^{90}Zr cross section for three energy bins of the GR peak and the continuum. The excitation energy in MeV of the center of the bin is shown. The lines through the data points indicate the multipole fits. Contributions of each multipole are shown [$L = 0$ red; $L = 1$, $T = 0$ black (dot); $L = 1$, $T = 1$ blue; $L = 2$ black (dash); $L = 3$ brown; $L = 4$ light green]. The statistical errors are shown, but in many cases are smaller than the data points.

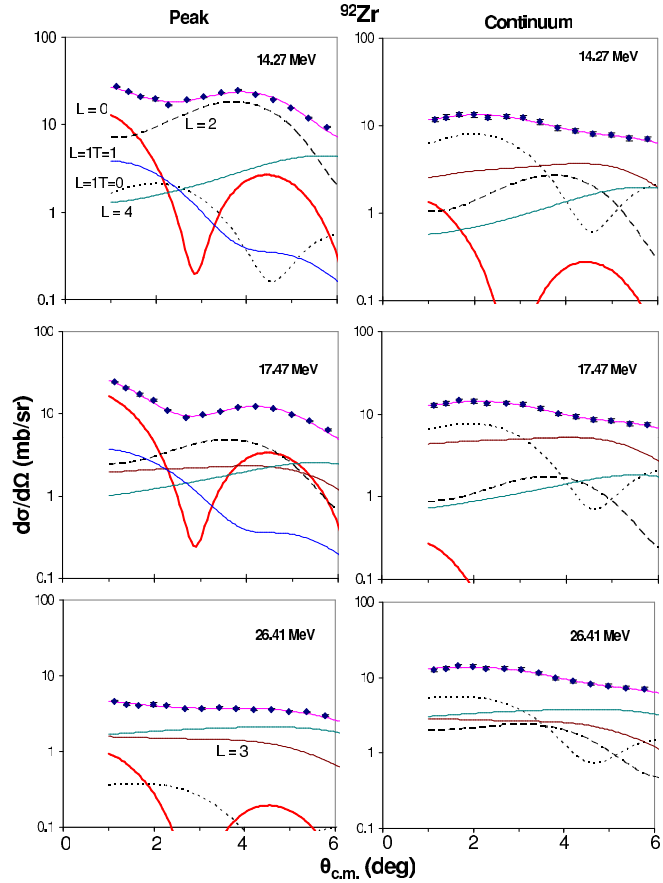

FIG. 3. (Color online) Same as Fig. 2 but for ^{92}Zr.

where $V_F(r)$ is the real single-folding potential obtained by folding the ground-state density with the density-dependent α-nucleon interaction,

$$v_{\mathrm{DDG}}(s,\rho) = -v[1 - \alpha\rho(r')^{\beta}]\exp[-s^2/t^2], \qquad (2)$$

where $s = |r - r'|$ is the distance between the center of mass of the α particle and a target nucleon, $\rho(r') = \rho_0(1 + e^{[(r'-c)/a]})^{-1}$ is the ground-state density of the target nucleus at the position r' of the target nucleon, $\alpha = 1.9\,\mathrm{fm}^2$, $\beta = 2/3$, and t (range) = 1.88 fm. W, R_i, and a_i are Woods-Saxon parameters for the imaginary potential. These calculations were carried out with the code PTOLEMY [32]. Since PTOLEMY calculates all kinematics nonrelativistically, corrections to the projectile mass and laboratory energy were made to achieve a proper relativistic calculation [33]. The shape of the real part of the potential and the form factor for PTOLEMY were obtained using the codes SDOLFIN and DOLFIN [34]. The transition densities and sum rules for various multipolarities are discussed thoroughly in Ref. [26] and, except for the ISGDR, the same expressions and techniques were used in this work. The transition density for inelastic α-particle excitation of the ISGDR given by Harakeh and Dieperink [35] (and described in Ref. [26]) is for only one magnetic substate, so that the transition density given in Ref. [26] must be multiplied by $\sqrt{3}$ in the DWBA calculations.

Samples of the angular distributions obtained for the giant resonance (GR) peak and the continuum are shown in Figs. 2–4 for ^{90}Zr, ^{92}Zr, and ^{94}Zr, respectively.

Fits to the angular distributions were carried out with a sum of isoscalar 0^+, 1^-, 2^+, 3^-, and 4^+ strengths. The isovector giant dipole resonance contributions were calculated from the known distribution [36] and were held fixed in the fits. Sample fits obtained, along with the individual components of the fits, are shown superimposed on the data in Figs. 2–4. The continuum distributions are similar over the entire energy range, whereas the angular distributions of the cross sections for the peak change as the contributions of different multipoles dominate in different energy regions.

Several analyses were carried out to assess the effects of different choices of the continuum on the resulting multipole distribution, as described in Ref. [18], where the continuum was systematically varied and the data were reanalyzed. The strength distributions obtained from these analyses using different choices of continuum were then averaged, and errors were calculated by adding the errors obtained from the multipole fits in quadrature to the standard deviations between the analyses with different continua. In general the $E0$ and

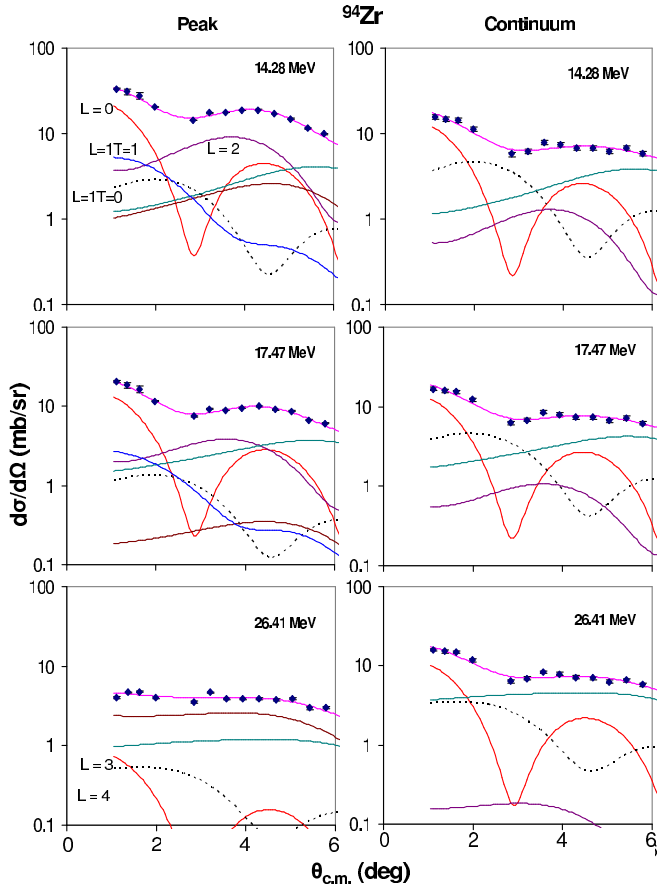

FIG. 4. (Color online) Same as Fig. 2 but for ^{94}Zr.

lower part of $E2$ distributions were relatively insensitive to the continuum choices, while the $E1$ and $E3$ distributions were more dependent on the continuum choices. This is reflected in the errors on the multipole distributions with the $E1$ distributions having the largest errors, and somewhat smaller errors on the $E3$ distributions. The errors on the $E0$ and $E2$ distributions are the smallest. The errors obtained in the multipole fits for a given continuum are approximately the same for each multipolarity (they are little larger for the $E1$ distribution), so that most of the difference is due to the effects of differing continuum choices. The isoscalar $E0$, $E1$, $E2$, and $E3$ distributions obtained for the GR peak are shown in Figs. 5–7, and the energies and sum-rule strengths obtained are summarized in Tables II–VI.

IV. DESCRIPTION OF MICROSCOPIC CALCULATIONS

The microscopic mean-field-based random-phase approximation (RPA) provides a good description of collective states in nuclei [24,38]. It is common to calculate the RPA strength function from

$$S(E) = \sum_n |\langle 0|F|n\rangle|^2 \delta(E - E_n), \tag{3}$$

where E_n is the energy of the RPA $|n\rangle$ state and $F = \sum_i f(r_i)Y_{L0}$ is the isoscalar ($T = 0$) single-particle scattering operator. We used $f(r) = r^2$ for the monopole ($L = 0$) and

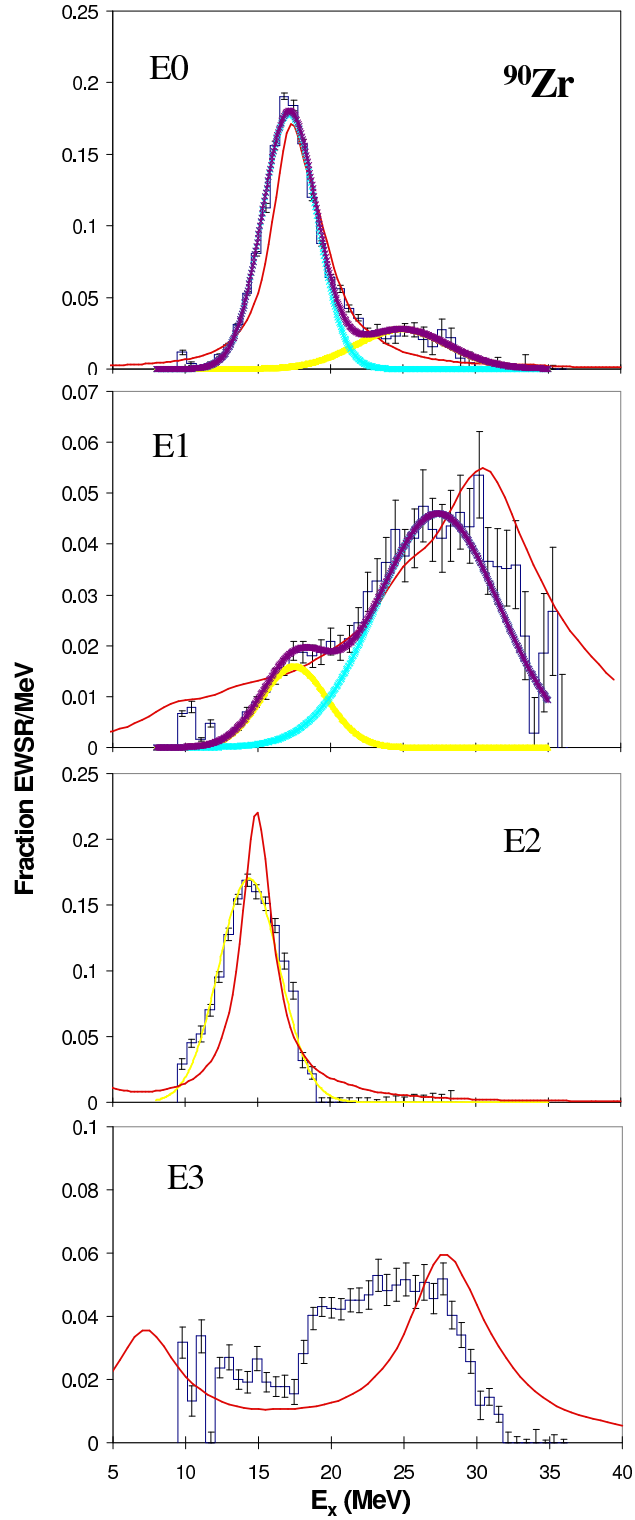

FIG. 5. (Color online) Isoscalar strength distributions obtained for ^{90}Zr are shown by the histograms. Error bars represent the uncertainty from the fitting of the angular distributions and different choices of the continuum, as described in the text. The thick lines in the $E0$ and $E1$ distributions represent the individual peaks and their sum obtained from the Gaussian fits (the blue and yellow lines are the individual peaks, while the brown line indicates the sum) The thin (red) lines are the strength distributions obtained with the HF-RPA calculations using the KDE0v1 interaction.

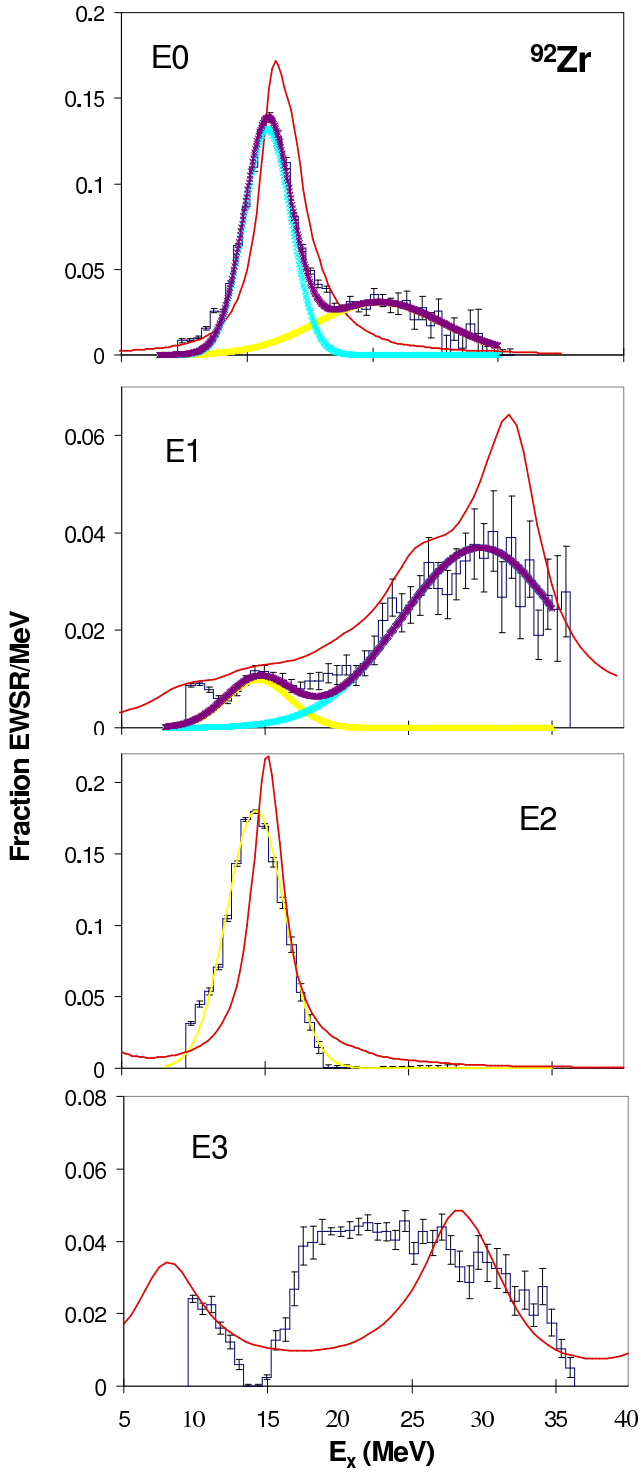

FIG. 6. (Color online) Same as Fig. 5 but for ^{92}Zr.

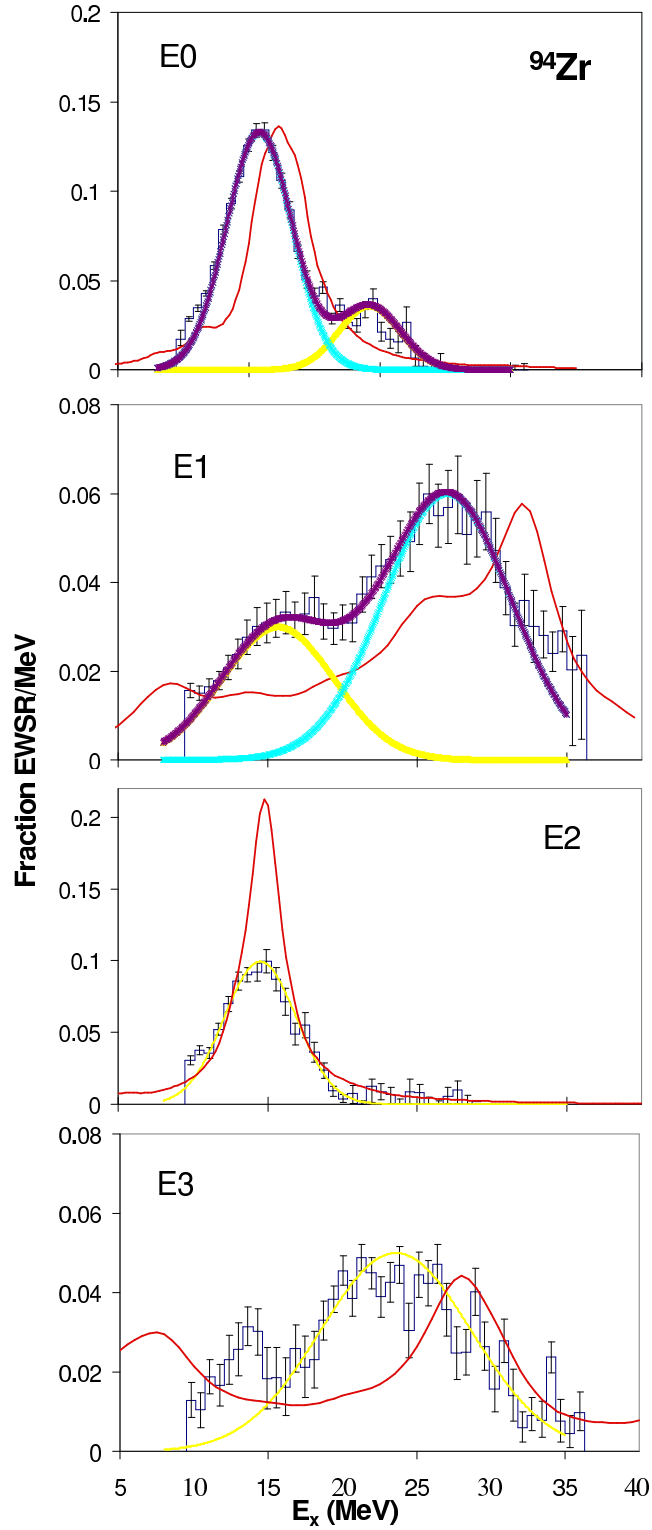

FIG. 7. (Color online) Same as Fig. 5 but for ^{94}Zr.

quadrupole ($L = 2$), $f(r) = r^3$ for the octupole ($L = 3$), and $f(r) = r^3 - \frac{5}{3}\langle r^2\rangle r$ for the dipole ($L = 1$) in order to account for contributions from the spurious state [39,40]. The energy moments can be determined using $m_k = \int E^k S(E) dE$. The constrained energy $E_{\rm con}$, centroid energy $E_{\rm cen}$, and the scaling energy E_s of the resonance are then given by $E_{\rm con} = (m_1/m_{-1})^{1/2}$, $E_{\rm cen} = m_1/m_0$, and $E_s = (m_3/m_1)^{1/2}$. The energy moment m_1 can also be calculated using the Hartree-Fock (HF) ground-state wave function, in order to calculate the energy-weighted sum rule (EWSR). Employing the theory discussed above and the numerical approach described in detail in Refs. [41–43], we carried out HF-based RPA calculations of the isoscalar strength functions and centroid energies for ^{90,92,94}Zr. We used an occupation number approximation for

TABLE II. Parameters obtained for the ISGMR (taken from Ref. [15]). Uncertainties include systematic errors.

	% $E0$ EWSR	m_1/m_0 (MeV)	rms width (MeV)	$(m_3/m_1)^{1/2}$ (MeV)	$(m_1/m_{-1})^{1/2}$ (MeV)	KDE0v1 $(m_3/m_1)^{1/2}$ (MeV)	KDE0v1 % E0 EWSR
^{90}Zr	106 ± 12	$17.88^{+0.13}_{-0.11}$	$3.69^{+0.33}_{-0.15}$	$18.86^{+0.23}_{-0.14}$	$17.58^{+0.06}_{-0.04}$	18.31	99.45
^{92}Zr	103 ± 12	$18.23^{+0.15}_{-0.13}$	$5.27^{+0.32}_{-0.25}$	$20.09^{+0.31}_{-0.22}$	$17.71^{+0.09}_{-0.07}$	18.35	99.44
^{94}Zr	106 ± 12	$16.16^{+0.12}_{-0.11}$	$4.13^{+1.02}_{-0.43}$	$17.52^{+0.18}_{-0.14}$	$15.75^{+0.27}_{-0.15}$	17.81	97.88
^{90}Zr[a]	100 ± 12	$17.81^{+0.32}_{-0.20}$	$3.55^{+0.60}_{-0.35}$	$18.69^{+0.65}_{-0.30}$	$17.55^{+0.25}_{-0.18}$		

[a]Reference [18].

the single-particle orbits of the open shell nuclei. As an example of theoretical predictions for giant resonances, within the HF-based RPA, we adopt the KDE0v1 effective Skyrme interaction [25]. This interaction was determined by a fit to extensive data on binding energies, charge radii of nuclei, single-particle spin-orbit splitting, and for the first time including the radii of valence single particle neutron orbits in ^{17}O and ^{43}Ca and the energies of the ISGMR in ^{90}Zr, ^{116}Sn, ^{144}Sm, and ^{208}Pb. Also included in the fit are additional constraints, such as the Landau stability conditions, positive derivative of the symmetry energy density at large density, and a minimal value for the enhancement factor of the energy weighted sum rule of the IVGDR. It is important to note that 240 Skyrme interactions, published in the literature, were analyzed by an independent group [44,45] for their ability to pass constraints relating to experimental data on properties of nuclear matter and nuclei, such as incompressibility coefficient, symmetry energy density, effective mass, binding energies, radii and fission barriers, and observational data of neutron stars. Only the KDE0v1 passed the tests. A more detailed comparison between theory and experiments, using over 30 Skyrme type interactions will be published soon [43]. The energies of the calculated strength functions were obtained using a small smearing width (0.1 MeV) to ensure accuracy and they are given in Tables II and IV–VI. We used the experimental excitation energy ranges: ISGMR 9-36 MeV, low component of ISGDR 9-20 MeV, high component of ISDGR 20-36 MeV, ISGQR 9-36 MeV, and ISGOR 15-36 MeV. The calculated distributions using smearing widths of $\Gamma = 10$ MeV for the ISGDR and $\Gamma = 5$ MeV for the other multipoles are shown superimposed on the experimental results in Figs. 5–7.

V. DISCUSSION

The $E0$–$E3$ multipole distributions obtained for ^{90}Zr, ^{92}Zr, and ^{94}Zr are shown in Figs. 5–7, respectively. Two peak fits are shown for the $E0$ and $E1$ distributions, while single Gaussian fits are shown for the $E2$ distributions for all nuclei and a single Gaussian fit is shown for the $E3$ distribution for ^{94}Zr. The $E0$ distributions have been reported previously [15] and the implications of these distributions, along with those of the Mo isotopes were explored. Values obtained for the parameters of the multipole distributions are given in Tables II and IV–VI along with the parameters obtained from the Gaussian fits. Each multipole is discussed separately below.

TABLE III. Gaussian fit parameters obtained for ISGMR distributions, taken from Ref. [15]. Uncertainties include systematic errors.

	Peak 1			Peak 2		
	EWSR (%)	Centroid (MeV)	FWHM (MeV)	EWSR (%)	Centroid (MeV)	FWHM (MeV)
^{90}Zr	84	17.1	4.4	22	24.9	7.6
^{92}Zr	62	16.6	4.4	38	25.5	12.0
^{94}Zr	83	15.8	5.9	21	24.2	5.6

A. $E0$ strength

The $E0$ distributions obtained for the three nuclei ^{90}Zr, ^{92}Zr, and ^{94}Zr have been previously reported [15] and are shown in Figs. 5–7. They consist of peaks around $E_x = 17.1$, 16.6, and 15.8 MeV, respectively, with a tail extending up to 30-35 MeV. Also shown in the figures are two-peak fits to the distributions. The $E0$ energy-weighted sum rule (EWSR) strengths obtained for these nuclei are $106 \pm 12\%$, $103 \pm 12\%$, and $106 \pm 12\%$, respectively. The origin of this high energy tail is not understood, but has been reported for ^{90}Zr in two previous experiments [18,21] and it's existence brought the value of K_{NM} (incompressibility of nuclear matter) extracted from the ^{90}Zr ISGMR energy in agreement with that obtained from heavier nuclei [21]. In ^{90}Zr the peak at $E_x \sim 24.9$ MeV contains $\sim$22% of the $E0$ EWSR while the lower peak contains the bulk of the $E0$ strength (84% EWSR). The results are in agreement with our two previous studies of $E0$ strength distribution of ^{90}Zr [18,21], where about $\sim$78% of the $E0$ strength was found in a symmetric peak at $E_x = 16.9$ MeV with the rest in a shoulder about 7 MeV higher in energy. The addition of two neutrons to ^{90}Zr results in a very different picture. In ^{92}Zr the higher peak at $E_x = 25.5$ MeV contains 38% and the lower narrow peak 62% of the $E0$ EWSR. The distribution of $E0$ strength in ^{94}Zr is similar to ^{90}Zr with the higher component containing 21% of the $E0$ strength whereas the lower peak contains 83% of $E0$ EWSR. The lower peak in ^{94}Zr is somewhat broader than in ^{90}Zr and ^{92}Zr, consistent with the trend in the Mo isotopes where the lower peak broadens considerably as the neutron number increases [15]. Reference [15] was the first report of the ISGMRs in ^{92}Zr and ^{94}Zr; however, the ISGMR in ^{90}Zr had been previously reported by a number of authors [46], but most of the studies did not do a multipole analysis, rather assuming that the ISGMR strength was contained in a Gaussian or Lorentzian peak, which was shown in Ref. [21] to be incorrect. ^{90}Zr ISGMR strength was extracted with 380 MeV α

TABLE IV. Gaussian fit parameters obtained for the ISGDR distributions. Uncertainties include systematic errors.

	Low energy peak			High energy peak			Total % $E1$	KDE0v1			
	Centroid (MeV)	FWHM (MeV)	% $E1$ EWSR	Centroid (MeV)	FWHM (MeV)	% $E1$ EWSR	seen in data EWSR	Low peak		High peak	
								m_1/m_0 (MeV)	% $E1$ EWSR	m_1/m_0 (MeV)	% $E1$ EWSR
^{90}Zr	17.5 ± 0.2	5.4 ± 0.7	9.2 ± 2.1	27.4 ± 0.5	10.1 ± 2.0	49 ± 6	64 ± 7	14.76	13.57	28.70	73.84
^{92}Zr	14.7 ± 0.3	5.4 ± 0.7	5.8 ± 1.2	30.0 ± 0.7	12.9 ± 2.0	51 ± 7	53 ± 6	14.38	12.68	28.41	73.51
^{94}Zr	15.7 ± 0.2	9.0 ± 1.0	28.0 ± 4.0	27.0 ± 0.5	9.9 ± 2.0	64 ± 7	96 ± 10	14.42	15.66	28.14	65.66
^{90}Zr[a]	17.1 ± 0.4	5.4 ± 0.3	13.0 ± 3.0	26.7 ± 0.5	8.8 ± 1.0	88 ± 9					
^{90}Zr[b]	17.8 ± 0.5	3.7 ± 1.2[c]	7.9 ± 2.9	26.9 ± 0.7	12.0 ± 1.5	67 ± 8					

[a]Reference [18].
[b]Reference [37], based on Breit-Wigner function fit.
[c]Width.

scattering at Osaka [37] using multipole analysis of the angular distributions obtained for specific energy bins and their result is compared to ours in Fig. 8. They see a continuous distribution of $E0$ strength above the peak extending to the highest energy they report, and the total $E0$ strength in their distribution, obtained by integration of the strength in the figure, is 123% of the $E0$ EWSR. This effect persists in other nuclei they have studied [47] where they see $E0$ strength extending up through the highest excitation energy they measure, with the total $E0$ strength considerably exceeding the sum rule. Their analyses do not include this high lying strength in their ISGMR parameters, and they conclude "The *raison dêtre* of this extra strength is not quite well understood" [47]. Thus we can draw no conclusions about the $E0$ strength above the peak from the Osaka work.

The HF-RPA calculations for $L = 0$ in Zr isotopes predict the strengths to be concentrated in a narrow band, and those are shown superimposed on the data in Figs. 5–7. The relevant scaling energy parameter $E_{\mathrm{GMR}} = (m_3/m_1)^{1/2}$ for each of Zr isotopes is shown in Fig. 9. Also shown in the figure are the ISGMR energies (E_{GMR}) for four Mo isotopes [48]. As we see in Fig. 9, the E_{GMR} for isobars (^{92}Zr and ^{92}Mo) are higher than values calculated with HF-RPA, which has been discussed in detailed in Ref. [15]. The calculated EWSR values for these nuclei are in good agreement with the observed values. The Gaussian centroids obtained for ^{90,92,94}Zr and 4 Mo isotopes ^{92,96,98,100}Mo [48] from the two-peak fits for the low and high components of the $E0$ distributions are plotted versus mass number (A) in Fig. 10. Also shown are lines representing $74/A^{1/3}$ and $111/A^{1/3}$ on the low and high component plots, indicating a possible $A^{-1/3}$ dependence of the energies. The energy of the higher peak is essentially constant (within errors) over the mass range 90–100; however, the energy of the lower peak clearly shows a decreasing trend with the mass number.

B. Isoscalar $E1$ strength

The total isoscalar dipole strength seen in ^{90,92,94}Zr is 64 ± 6%, 53 ± 6%, and 96 ± 10%, respectively, of the EWSR, distributed between two peaks separated by 10–15 MeV. The isoscalar dipole is split into $1\hbar\omega$ and $3\hbar\omega$ components [19,49,50] and the upper component is expected to be a compression mode whose energy is related to the compression modulus K_A of the nucleus. Two peak Gaussian fits to the strength distributions are shown in Figs. 5–7 and the parameters obtained are listed in Table IV and compared to those obtained previously for ^{90}Zr [18,37]. For ^{90}Zr, the energies obtained in this work for both components agree well with both our previous work [18] and the Osaka work [37]; however, the $E1$ strength identified in this work is lower. In our previous work, both horizontal and vertical angles were measured in the focal plane [18] resulting in better angle resolution and an expanded angle range, particularly toward 0°, which may have aided in separating the $E1$ strength from the continuum. There are no previous reports of the ISGDR in ^{92,94}Zr.

HF-RPA calculations with the KDE0v1 interaction are shown superimposed on the multipole distributions in Figs. 5–7 and the parameters obtained are listed in Table IV.

TABLE V. Parameters obtained for the ISGQR distributions. Uncertainties include systematic errors.

	Moments			Gaussian fits		KDE0v1	
	% $E2$ EWSR	m_1/m_0 (MeV)	rms width (MeV)	Centroid (MeV)	FWHM (MeV)	m_1/m_0 (MeV)	% $E2$ EWSR
^{90}Zr	92 ± 12	14.09 ± 0.20	2.09 ± 0.20	14.56 ± 0.20	4.94 ± 0.20	15.27	93.55
^{92}Zr	93 ± 12	14.16 ± 0.21	3.86 ± 0.40	14.35 ± 0.15	4.8 ± 0.2	15.28	93.56
^{94}Zr	67 ± 11	14.08 ± 0.22	2.49 ± 0.30	14.49 ± 0.15	5.7 ± 0.3	14.56	97.16
^{90}Zr[a]	88 ± 10	14.30 ± 0.12	2.14 ± 0.25	14.65 ± 0.20	4.9 ± 0.2		

[a]Reference [18].

TABLE VI. Parameters obtained for the isoscalar ISGOR strength above $E_x = 12$–15 MeV (see text). Uncertainties include systematic errors.

	% $E3$ EWSR	m_1/m_0 (MeV)	rms width (MeV)	KDE0v1	
				m_1/m_0 (MeV)	% $E3$ EWSR
^{90}Zr	59 ± 8	23.1 ± 0.4	3.8 ± 0.3	26.98	63.89
^{92}Zr	69 ± 9	23.9 ± 0.4	5.3 ± 0.3	26.96	63.16
^{94}Zr	58 ± 8	23.6 ± 0.4	4.84 ± 0.30	26.18	59.75
^{90}Zr[a]	78^{+9}_{-15}	$22.91^{+0.70}_{-0.50}$	$4.27^{+0.60}_{-0.45}$		

[a]Reference [18].

The HF-RPA calculations show 13–16% of the ISGDR EWSR in the lower component with $m_1/m_0 = 14.4$–14.8 MeV and 66–74% of the ISGDR EWSR in the higher component with $m_1/m_0 = 28.1$–28.7 MeV.

The strength and Gaussian centroids of the high energy peaks for Zr isotopes (present work) and Mo isotopes [48] are compared to those obtained from the HF-RPA calculations in Fig. 11. The energies obtained for the high energy peaks for ^{90,94}Zr and ^{92}Mo are 1.0–1.5 MeV below the calculated energies, whereas those for ^{92}Zr and ^{96,98}Mo are about the same amount above the calculated values. The energy for ^{98}Mo is <1 MeV lower than the calculated value, and essentially is within the experimental error. The strength seen in the upper peak is substantially lower than that predicted by the calculation except for ^{94}Zr and ^{96}Mo.

In a recent study on ^{90}Zr, isoscalar dipole strength at low energy has been investigated using the (^{17}O,^{17}O$'\gamma$) [51] reaction. Approximately ~2.1% of the sum rule was identified. In our HF-RPA calculations, there is also some dipole strength below 8 MeV.

C. $E2$ strength

The $E2$ strengths in ^{90}Zr, ^{92}Zr, and ^{94}Zr are concentrated in (almost) Gaussian peaks having $m_1/m_0 \sim 14.1$ MeV containing $92 \pm 12\%$, $93 \pm 12\%$, and $67 \pm 11\%$ of the $E2$ EWSR. For ^{90}Zr, m_1/m_0, the Gaussian centroid, the width,

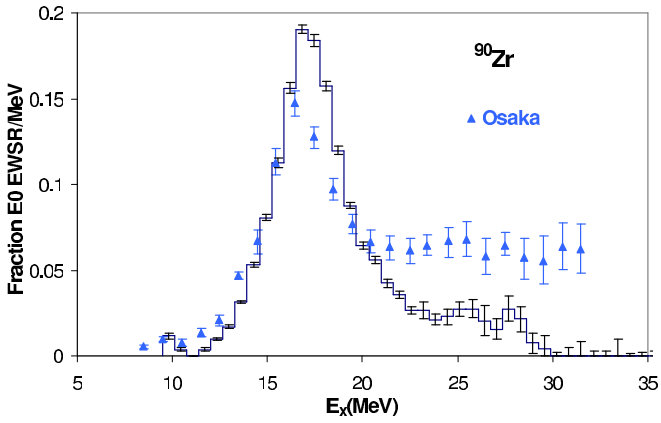

FIG. 8. (Color online) Comparison of ISGMR strength distribution for ^{90}Zr obtained in this work with that reported by Osaka [37].

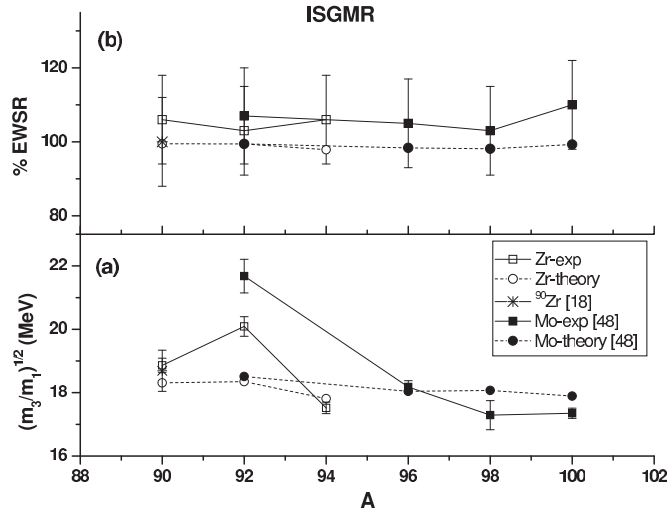

FIG. 9. The scaling energy parameter $E_{\rm GMR} = (m_3/m_1)^{1/2}$ and strength in Zr (this work) and Mo [48] isotopes are shown in the lower (a) and upper (b) panels, respectively. The error bars indicate the uncertainty obtained using the errors shown in Figs. 5–7. The calculated values using HF-RPA model are also shown.

and the strength are all in excellent agreement with our previous work [18]. The position is in agreement with work by Buenerd *et al.* [52] and Borghols *et al.* [53]; however, Buenerd *et al.* reported observing only 51% of the EWSR and Borghols reported a width of 3.0 ± 0.5 MeV. The parameters obtained for the $E2$ distributions and the results from the HF-RPA calculations are given in Table V.

The energies and strengths of the $E2$ distributions in the Zr and Mo nuclei are compared to the HF-RPA calculations in Fig. 12. The centroid energies (m_1/m_0) obtained with the HF-RPA calculations are ~1.2 MeV (5σ) higher than the

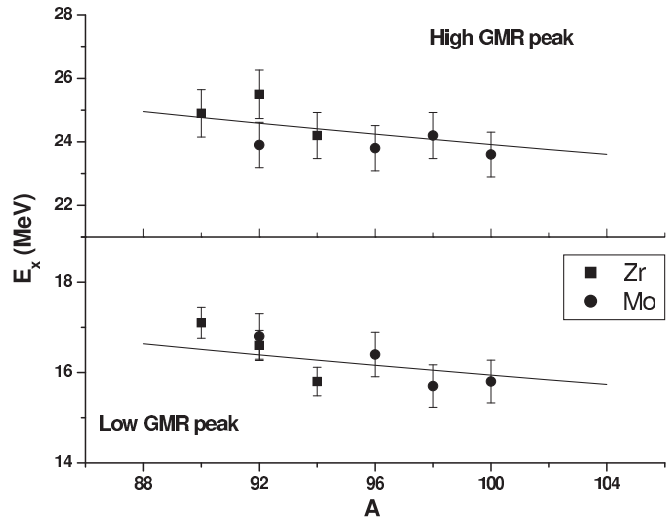

FIG. 10. The centroid energies of the Gaussian fits obtained for the $E0$ distributions for Zr (this work) and Mo [48] are plotted vs mass number (A). The error bars indicate the uncertainty obtained using the errors shown in Figs. 5–7. The lines show $74 \times A^{-1/3}$ and $111 \times A^{-1/3}$ for the lower (a) and upper (b) plots, respectively.

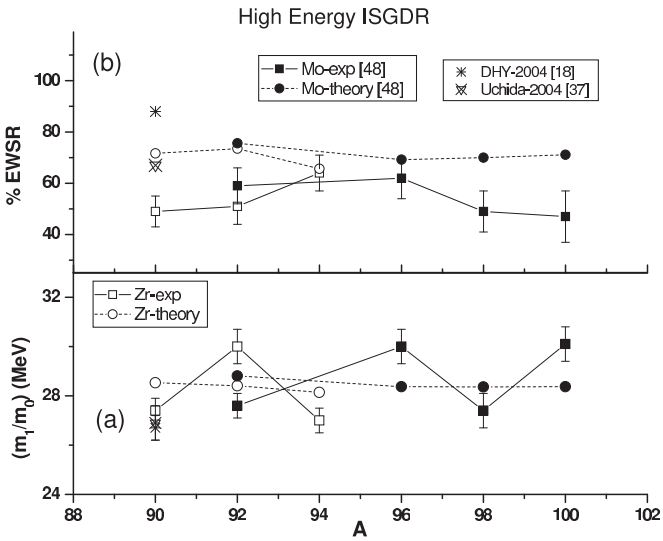

FIG. 11. The centroid of the Gaussian fit to the high energy peak in the ISGDR distributions for each of the Zr (this work) and Mo [48] isotopes is plotted vs mass number (A) in the lower panel (a), while the strength in the upper peak is plotted in the upper panel (b). The error bars indicate the uncertainty obtained using the errors shown in Figs. 5–7.

experimental values for ^{90,92}Zr and ∼0.4 MeV higher (2σ) for ^{94}Zr. Essentially all of the expected $E2$ strength is seen in ^{90,92}Zr, but in ^{94}Zr only about ∼65% of the expected strength was located. A similar trend for m_1/m_0 is also apparent for the Mo isotopes [48] where the HF-RPA values are 4σ–5σ above the experimental values.

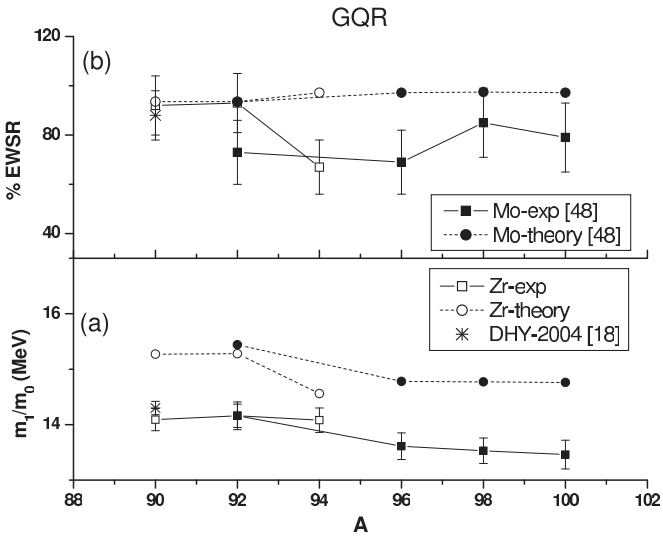

FIG. 12. The centroids and the strengths of the $E2$ distribution in Zr (this work) and Mo isotopes [48] are plotted against the mass number (A) in the lower (a) and upper (b) panels, respectively. The error bars indicate the uncertainty obtained using the errors shown in Figs. 5–7. Also shown by the circles are the values obtained from HF-RPA calculations with the KDE0v1 interaction.

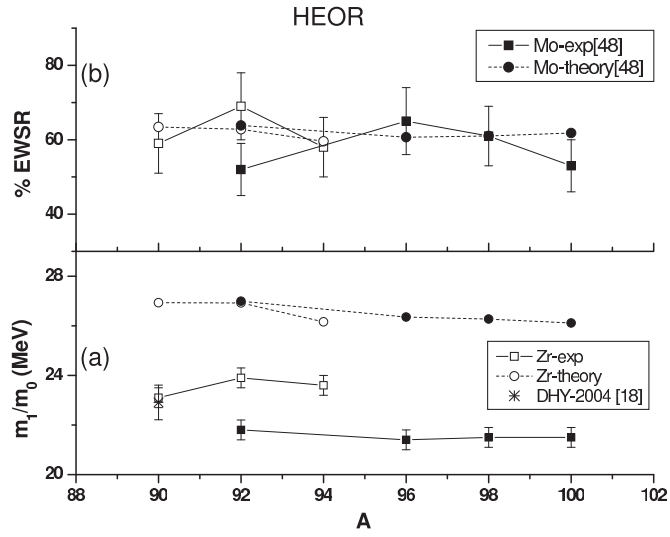

FIG. 13. The centroid of the $E3$ strength observed above $E_x = 15$ MeV for each of the Zr (this work) and Mo ([48]) isotopes is plotted vs A in the lower panel (a), while the strength in this region is plotted in the upper panel (b). The error bars indicate the uncertainty obtained using the errors shown in Figs. 5–7. Empty circles show the centroid and strength of $E3$ distribution in Zr isotopes between $E_x = 15$ and 35 MeV obtained from the HF-RPA calculations with the KDE0v1 interaction.

D. $E3$ strength

The $E3$ strength is generally split into a $1\hbar\omega$ LEOR containing 25% of the isoscalar $E3$ EWSR and a $3\hbar\omega$ HEOR containing 75% of the EWSR [12,54]. Our low energy cutoff in this experiment lies in the middle to higher region of the LEOR, so that we are unable to extract useful parameters for the LEOR. The observed $E3$ strength distributions are broadly spread from $E_x \sim 9$ MeV (the lower threshold of our detector) and tapering off between $E_x = 30$–35 MeV before reaching the upper limit of the region we observe ($E_x = 36$ MeV). If we arbitrarily choose the division between the LEOR and HEOR at $E_x = 12$–15 MeV, depending on the apparent gap in the strength distributions, for the HEOR in ^{90}Zr, ^{92}Zr, and ^{94}Zr, m_1/m_0 is 23.1, 23.9, and 23.6 MeV, the rms widths are 3.8, 5.3, 4.84 MeV and 59%, 69%, and 58% of the $E3$ EWSR is observed, respectively. In our earlier work on ^{90}Zr [18] we reported $E3$ strength having $m_1/m_0 = 22.91^{+0.70}_{-0.50}$ MeV, an rms width of $4.27^{+0.60}_{-0.45}$ MeV and 78^{+9}_{-15}% of the $E3$ EWSR in agreement within errors with this result. The parameters obtained for the HEOR are given in Table VI. In a much earlier work where a multipole decomposition was not done, Bertrand *et al.* [55] using 200 MeV proton scattering, and fitting multiple Gaussians to the spectrum after subtracting a continuum, reported an $L = 3$ peak at 27 ± 1 MeV with a width of 9 ± 1 MeV, but did not report the EWSR fraction. There are no previous reports of the HEOR in ^{92,94}Zr. The isoscalar $E3$ strength calculated with the KDE0v1 interaction is also shown in Figs. 5–7 and has peaks at ∼8 MeV (the LEOR) and at ∼27 MeV (the HEOR) whereas the experimental strength lies in a broad peak centered at ∼23–24 MeV. The experimental and calculated energies and strengths are compared for the

HEOR in Fig. 13 along with data for Mo isotopes [48]. The experimental excitation energies (m_1/m_0) are ∼2.6–4.0 MeV below those obtained with the HF-RPA calculations, while in the Mo isotopes [48] the difference was larger (∼4 MeV).

The strength seen in the HEOR agrees within the errors with the HF-RPA calculations for the Zr and Mo [48] isotopes except for ^{92}Mo where the experimental strength is somewhat below the prediction.

VI. SUMMARY

Most of the expected isoscalar $E0$–$E3$ strength (58–106%) in ^{90,92,94}Zr has been identified using inelastically scattered 240 MeV α particles. The strength distributions are compared with Hartree-Fock based RPA calculations using the KDE0v1 Skyrme type interaction. As discussed in a previous report [15], the $E0$ strength consists of a relatively narrow peak, with significant tailing at higher excitation, which contains a substantially larger fraction of the $E0$ strength in ^{92}Zr and ^{92}Mo than in the other Zr and Mo isotopes. This high energy tail shifts the ISGMR energy higher for ^{92}Zr and ^{92}Mo, which is not seen in the HF-RPA calculations. The source of this "tail," not present in heavier nuclei, is not understood, and the distributions for other multipoles do not differ substantially between the isotopes. The positions of the high energy part of the isoscalar dipole in ^{90,92}Zr are about 1.2 MeV below those obtained with the KDE0v1 interaction, while for ^{94}Zr the experimental value is about 1.6 MeV above the calculated value. The $E2$ strength in the Zr isotopes is concentrated in almost Gaussian peaks having m_1/m_0 ∼ 14.1 MeV, for ^{90,92}Zr ∼1.2 MeV and ^{94}Zr ∼0.5 MeV below those obtained with HF-RPA calculations. The HEOR strength lies in a broad peak having E_x ∼ 23–24 MeV in the three isotopes, 2.5–2.9 MeV below those obtained with the KDE0v1 interaction.

ACKNOWLEDGMENT

This work was supported in part by the US Department of Energy under the grant DE-FG03-93ER40773.

[1] G. C. Baldwin and G. S. Klaiber, Phys. Rev. **71**, 3 (1947).
[2] R. Pitthan and Th. Walcher, Z. Naturforsch. A **27**, 1683 (1972).
[3] L. L. Rutledge and J. C. Hiebert, Phys. Rev. Lett. **32**, 551 (1974).
[4] J. M. Moss, C. M. Rozsa, J. D. Bronson, and D. H. Youngblood, Phys. Lett. B **53**, 1 (1974).
[5] N. Marty, M. Morlet, A. Willis, V. Comparat, and R. Frascaria, in *Proceedings of the International Symposium on Highly Excited States in Nuclei*, Julich (RFA), Vol. 1, edited by A. Faessler, P. Mayer-Boricke, and P. Turek (Zentralbibliothek der Kernforschungsanlage, Julich, 1975), p. 17.
[6] S. Fukuda and Y. Torizuka, Phys. Lett. B **62**, 146 (1976); M. Sasao and Y. Torizuka, Phys. Rev. C **15**, 217 (1977).
[7] M. N. Harakeh, K. van der Borg, T. Ishimatsu, H. P. Morsch, A. van der Woude, and F. E. Bertrand, Phys. Rev. Lett. **38**, 676 (1977).
[8] D. H. Youngblood, C. M. Rozsa, J. M. Moss, D. R. Brown, and J. D. Bronson, Phys. Rev. Lett. **39**, 1188 (1977).
[9] M. Nagao and Y. Torizuka, Phys. Rev. Lett. **30**, 1068 (1973).
[10] T. A. Carey, W. D. Cornelius, N. J. DiGiacomo, J. M. Moss, G. S. Adams, J. B. McClelland, G. Pauletta, C. Whitten, M. Gazzaly, N. Hintz, and C. Glashausser, Phys. Rev. Lett. **45**, 239 (1980).
[11] H. P. Morsch, M. Rogge, P. Turek, and C. Mayer-Boricke, Phys. Rev. Lett. **45**, 337 (1980).
[12] J. M. Moss, D. H. Youngblood, C. M. Rozsa, D. R. Brown, and J. D. Bronson, Phys. Rev. Lett. **37**, 816 (1976).
[13] J. P. Blaizot, J. F. Berger, J. Decharge, and M. Girod, Nucl. Phys. A **591**, 435 (1995).
[14] J. P. Blaizot, Phys. Rep. **64**, 171 (1980).
[15] D. H. Youngblood, Y.-W. Lui, Krishichayan, J. Button, M. R. Anders, M. L. Gorelik, M. H. Urin, and S. Shlomo, Phys. Rev. C **88**, 021301(R) (2013).
[16] Y.-W. Lui, D. H. Youngblood, S. Shlomo, X. Chen, Y. Tokimoto, Krishichayan, M. Anders, and J. Button, Phys. Rev. C **83**, 044327 (2011).
[17] Y.-W. Lui, D. H. Youngblood, H. L. Clark, Y. Tokimoto, and B. John, Phys. Rev. C **73**, 014314 (2006); D. H. Youngblood, Y.-W. Lui, H. L. Clark, B. John, Y. Tokimoto, and X. Chen, *ibid.* **69**, 034315 (2004).
[18] D. H. Youngblood, Y.-W. Lui, B. John, Y. Tokimoto, H. L. Clark, and X. Chen, Phys. Rev. C **69**, 054312 (2004).
[19] H. L. Clark, Y.-W. Lui, and D. H. Youngblood, Phys. Rev. C **63**, 031301(R) (2001).
[20] D. H. Youngblood, Y.-W. Lui, H. L. Clark, Y. Tokimoto, and B. John, Phys. Rev. C **68**, 057303 (2003).
[21] D. H. Youngblood, H. L. Clark, and Y.-W. Lui, Phys. Rev. Lett. **82**, 691 (1999).
[22] D. H. Youngblood, Y.-W. Lui, and H. L. Clark, Phys. Rev. C **65**, 034302 (2002).
[23] D. H. Youngblood, Y.-W. Lui, and H. L. Clark, Phys. Rev. C **63**, 067301 (2001).
[24] S. Shlomo, V. M. Kolomietz, and G. Colo, Eur. Phys. J. A **30**, 23 (2006), and references therein.
[25] B. K. Agrawal, S. Shlomo, and V. K. Au, Phys. Rev. C **72**, 014310 (2005).
[26] D. H. Youngblood, Y.-W. Lui, and H. L. Clark, Phys. Rev. C **55**, 2811 (1997).
[27] D. H. Youngblood, Y.-W. Lui, and H. L. Clark, Phys. Rev. C **60**, 014304 (1999).
[28] K. van der Borg, M. N. Harakeh, and A. van der Wounde, Nucl. Phys. A **365**, 243 (1981).
[29] H. L. Clark, Y.-W. Lui, and D. H. Youngblood, Nucl. Phys. A **687**, 80c (2001).
[30] G. R. Satchler and D. T. Khoa, Phys. Rev. C **55**, 285 (1997).
[31] H. L. Clark, Y.-W. Lui, and D. H. Youngblood, Phys. Rev. C **57**, 2887 (1998).
[32] M. Rhoades-Brown, M. H. Macfarlane, and S. C. Pieper, Phys. Rev. C **21**, 2417 (1980); M. H. Macfarlane and S. C. Pieper, Argonne National Laboratory Report No. ANL-76-11, 1978 (unpublished).
[33] G. R. Satchler, Nucl. Phys. A **540**, 533 (1992).

[34] L. D. Rickerston, the folding program DOLFIN, 1976 (unpublished).
[35] M. N. Harakeh and A. E. L. Diepernik, Phys. Rev. C **23**, 2329 (1981)
[36] S. S. Dietrich and B. L. Berman, At. Data Nucl. Data Tables **38**, 199 (1988).
[37] M. Uchida *et al.*, Phys. Rev. C **69**, 051301 (2004).
[38] A. Bohr and B. M. Mottelson, *Nuclear Structure II* (Benjamin, New York, 1975).
[39] S. Shlomo and A. I. Sanzhur, Phys. Rev. C **65**, 044310 (2002).
[40] B. K. Agrawal, S. Shlomo, and A. I. Sanzhur, Phys. Rev. C **67**, 034314 (2003).
[41] P.-G. Reinhardt, Ann. Phys. (Leipzig) **1**, 632 (1992).
[42] T. Sil, S. Shlomo, B. K. Agarwal, and P.-G. Reinhard, Phys. Rev. C **73**, 034316 (2006).
[43] G. Bonasera *et al.* (unpublished).
[44] M. Dutra, O. Lourenco, J. S. Sa Martins, A. Delfino, J. R. Stone, and P. D. Stevenson, Phys. Rev. C **85**, 035201 (2012).
[45] P. D. Stevenson, P. D. Goddard, J. R. Stone, and M. Dutra, AIP Conf. Proc. **1529**, 262 (2013).
[46] M. N. Harakeh and A. van der Woude, *Giant Resonances: Fundamental High-Frequency Modes of Nuclear Excitation* (Oxford University Press, New York, 2001).
[47] T. Li *et al.*, Phys. Rev. C **81**, 034309 (2010).
[48] D. H. Youngblood, Y.-W. Lui, Krishichayan, J. Button, G. Bonasera, and S. Shlomo, Phys. Rev. C **92**, 014318 (2015).
[49] G. Colo, N. Van Giai, P. F. Bortignon, and M. R. Quaglia, Phys. Lett. B **485**, 362 (2000).
[50] D. Vretenar, A. Wandelt, and P. Ring, Phys. Lett. B **487**, 334 (2000).
[51] F. C. L. Crespi *et al.*, Phys. Rev. C **91**, 024323 (2015).
[52] M. Buenerd, C. Bonhomme, D. Lebrun, P. Martin, J. Chauvin, G. Duhamel, G. Perrin, and P. de Saintignon, Phys. Lett. B **84**, 305 (1979).
[53] W. T. A. Borghols *et al.*, Nucl. Phys. A **504**, 231 (1989).
[54] J. M. Moss, D. R. Brown, D. H. Youngblood, C. M. Rozsa, and J. D. Bronson, Phys. Rev. C **18**, 741 (1978).
[55] F. E. Bertrand, E. E. Gross, D. J. Horen, J. R. Wu, J. Tinsley, D. K. McDaniels, L. W. Swenson, and R. Lijestrand, Phys. Lett. B **103**, 326 (1981).